

Imaging of Metal Impurities in Silicon by Luminescence Spectroscopy and Synchrotron Techniques

MARTIN C. SCHUBERT^{1,2} JONAS SCHÖN,¹ PAUL GUNDEL,¹
HOLGER HABENICHT,¹ WOLFRAM KWAPIL,¹
and WILHELM WARTA¹

1.—Fraunhofer Institute for Solar Energy Systems, Heidenhofstr. 2, 79110 Freiburg, Germany.
2.—e-mail: martin.schubert@ise.fraunhofer.de

Metals are detrimental to silicon solar cells in two ways: (i) they typically introduce defect levels in the bandgap, leading to enhanced carrier recombination and thus to lower voltage in solar cells; and (ii) they may, in the form of precipitates, contribute to the formation of shunts and reverse breakdown sites. This paper provides a review on techniques to access the spatial distribution of recombination sites for multicrystalline silicon. Methods to detect metal precipitates as well as, in the case of iron, dissolved point defects are presented. These methods are applied to clarify the distribution of iron after high-temperature processes and the identification of breakdown sites.

Key words: Multicrystalline silicon, solar cells, transition metals, luminescence, synchrotron

INTRODUCTION

Metals, dissolved as point defects or clustered in the form of precipitates, reduce the carrier lifetime in multicrystalline (mc) silicon (Fig. 1). Introduced with the silicon feedstock before crystallization or within the crystallization process due to outdiffusion from crucible walls, metals have a detrimental effect on the efficiency of multicrystalline silicon solar cells.

Extensive research on the distribution and concentration of metals in multicrystalline silicon as well as on gettering of metals (see, e.g., Refs. 2–7) has been performed in the past. Imaging of metallic impurities has turned out to provide very valuable information about the behavior of metals. Without attempting to be complete, we will present a variety of mapping and imaging techniques which access the spatial distribution of metallic impurities. Together with numerical simulations in one and two dimensions we demonstrate effects of dissolution and precipitation in both industrial-type multicrystalline silicon and model systems with intentionally contaminated dislocation networks.

In addition to these recombination-related experiments we emphasize the role of metal precipitates for the reverse current, namely breakdown sites in solar cells. Breakdown sites may be detrimental for solar modules due to a possible strong temperature increase which may yield to thermal destruction of a module (Fig. 2).

DETECTION OF LUMINESCENCE FOR MATERIAL CHARACTERIZATION

Photoluminescence Imaging

Although band-to-band (BB) recombination of silicon is low compared with Shockley–Read–Hall recombination via deep defect levels, measurement of the photoluminescence (PL) signal has turned out to be a sensitive means to probe the recombination lifetime.⁸ PL imaging⁹ in particular is a very fast and easy technique to image lifetime with high spatial resolution.

In addition to lifetime, the concentration of iron point defects can be quantitatively determined by means of PL imaging. Following an idea of Zoth and Bergholz,¹⁰ lifetime before and after light soaking is compared. Light soaking changes the chemical state of iron point defects from a state bound to boron to

(Received September 19, 2009; accepted February 5, 2010;
published online March 3, 2010)

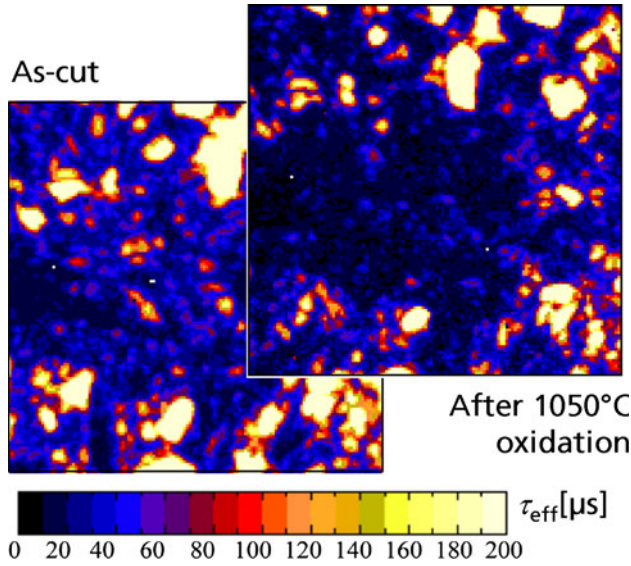


Fig. 1. Influence of a high-temperature step on recombination lifetime in multicrystalline silicon. Oxidation at 1050°C results in a severe decrease of material quality.¹

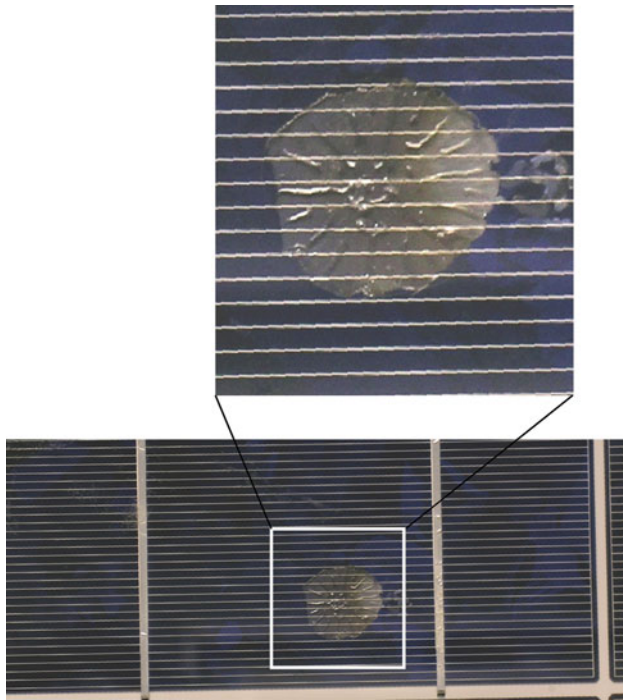


Fig. 2. Section of a damaged silicon solar cell module due to a hot spot. Highly localized power dissipation results in thermal degradation of the module.

an interstitial state. Since the recombination properties differ significantly (Fig. 3), the concentration of iron point defects can be determined. Macdonald et al.¹¹ have adapted this approach for analysis at constant generation rate instead of constant injection level in order to meet the requirements for

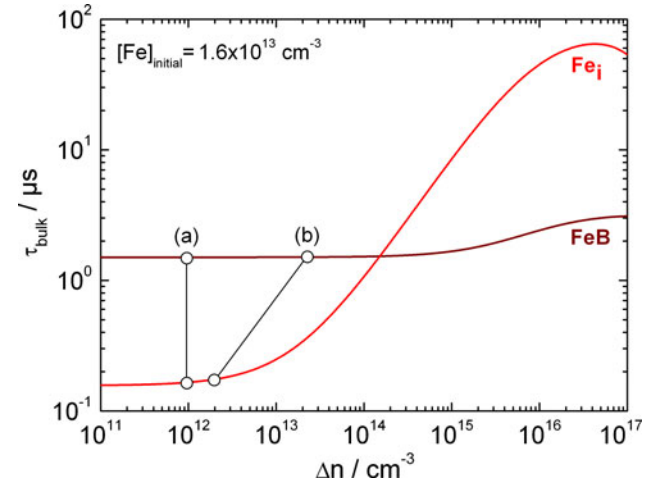


Fig. 3. Injection-dependent lifetime curves for iron point defects in the interstitial state (Fe_i) and bound to boron (FeB). Comparison of lifetime measurements in the two states enables determination of the quantitative density of iron point defects. The calculation can be performed under (a) constant-injection conditions or (b) constant-generation conditions.

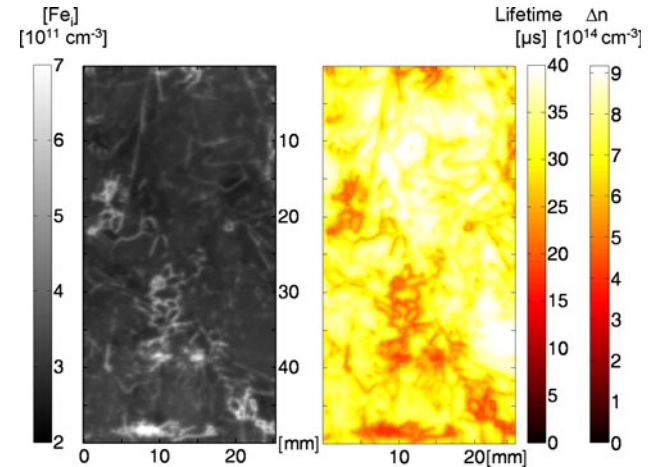


Fig. 4. Image of iron point defect density and comparison with PL lifetime image. A scale for the injection level is added to the lifetime image.

camera-based measurements at homogeneous and constant illumination intensity.

The analysis assumes that the injection level is constant to a good approximation over the wafer thickness. A study of the conditions under which this assumption is valid may be found in Ref. 12.

An example of iron imaging is shown in Fig. 4 (left). Comparison with the recombination lifetime image reveals a correlation between high interstitial iron concentration and reduced lifetime.

Photoluminescence Spectroscopy

The spatial resolution of photoluminescence measurements can be pushed further by replacing

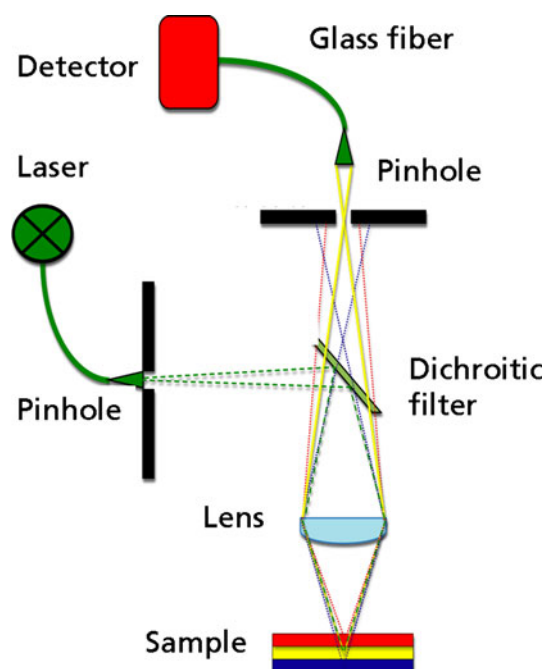


Fig. 5. Setup for confocal photoluminescence spectroscopy. A laser of 532 nm wavelength illuminates the sample. The PL spectrum is detected by an InGaAs-camera array.^{13,14}

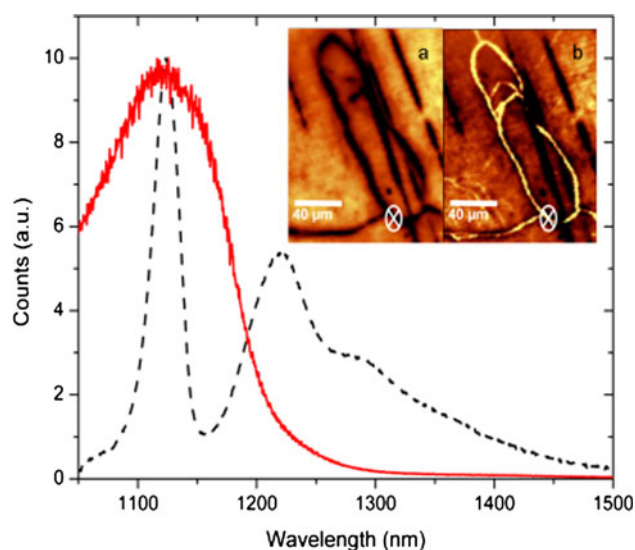


Fig. 6. Example photoluminescence spectrum from multicrystalline silicon at 77 K. The inserts show the spatial distribution of the band-to-band luminescence (integrated between 1070 nm and 1210 nm), indicating recombination sites and defect luminescence [fit with peak at 1250 nm (0.99 eV)] at room temperature.¹⁴ The position where the spectra were recorded is indicated in the images.

the camera setup by a confocal microscope. Whereas for the first method a resolution of several tens of microns is typical, submicron resolution is obtained by the latter method. A laser of 532 nm wavelength is used for carrier generation. The luminescence

spectrum is recorded via an InGaAs-camera array (Fig. 5). A typical spectrum on multicrystalline silicon at 77 K is shown in Fig. 6. The inserted maps in Fig. 6 show the band-to-band (BB) and defect luminescence. Recombination active defects can be localized with resolution of approximately 1 μm .

SYNCHROTRON TECHNIQUES

In addition to the study of the luminescence properties of silicon, x-ray fluorescence (XRF) analysis provides insight into the distribution and chemical composition of metal precipitates. This method has been very successfully applied to multicrystalline silicon.¹⁵ In this paper $\mu\text{-XRF}$ measurements serve to localize and identify metal precipitates in silicon samples with decorated dislocation networks. These networks have been obtained by direct wafer bonding¹⁶ of two floatzone (FZ) wafers under a small twisting angle. After annealing to obtain covalent atomic bonding, the wafer has been intentionally contaminated with iron.

The intensity of the Fe K_{α} line of this wafer has been mapped at the ID22 beamline at the European Synchrotron Radiation Facility (ESRF) synchrotron. When compared with a map of the BB luminescence obtained with the confocal photoluminescence spectroscopy setup (Fig. 5), good correlation between detected iron precipitates and localized recombination sites is obtained. The PL mapping offers significantly better spatial resolution and sensitivity than the $\mu\text{-XRF}$ measurement, but has two limitations: (i) the chemical nature of the detected recombination sites cannot be determined, and (ii) the analysis of recombination activity is restricted to the first few microns of the wafer thickness, as is apparent by comparing the area marked by the dashed circle: although an iron precipitate has been identified by $\mu\text{-XRF}$ spectroscopy, no recombination site is detected in the PL mapping. First indications of differences in the defect spectrum at longer wavelengths¹³ may be a means to distinguish between different metal species. The information depth of the PL mapping may be increased by the use of a laser with longer wavelength.

A new method for silicon characterization *in situ* with $\mu\text{-XRF}$ measurements is shown in Fig. 8. X-ray excited optical luminescence spectroscopy (XEOL)^{17,18} has been applied to silicon.¹⁹ Although PL spectroscopy is a more sensitive technique, XEOL enables direct characterization of recombination activity together with the distribution of metal precipitates. This may, after optimization of the sensitivity, offer better orientation on the sample and point-by-point comparison of recombination activity and metal precipitate distribution. In contrast to x-ray beam induced current (XBIC),²⁰ no metal contacts, which may increase the background signal, are necessary for this technique.

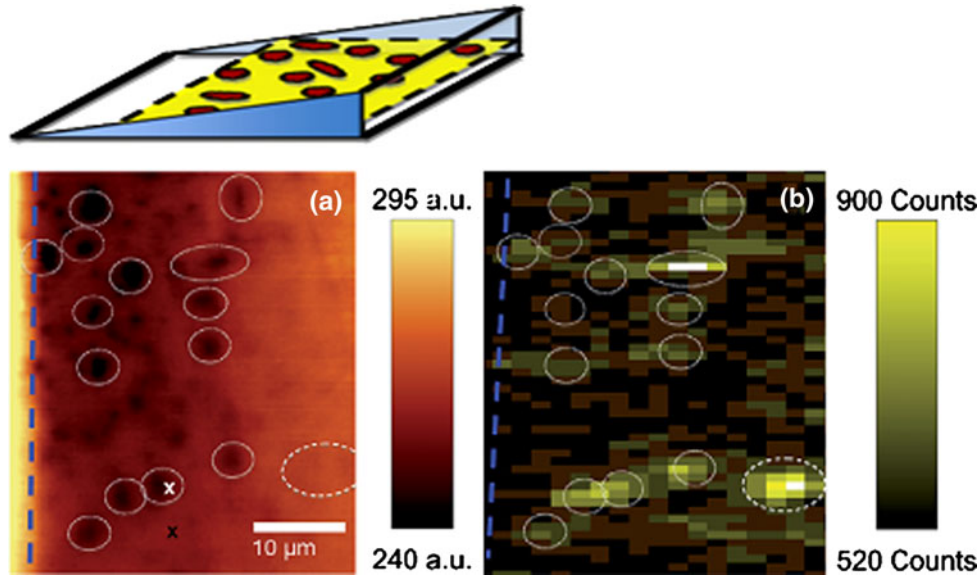


Fig. 7. (a) PL mapping (BB luminescence) of dislocation network decorated with iron precipitates measured with the setup shown in Fig. 5. (b) μ -XRF mapping of Fe K _{α} line, measured at the ESRF synchrotron. The detected iron precipitates correlate well with the photoluminescence mapping. The latter exhibits even better resolution but does not give indications about the chemical composition of the precipitates. The current PL setup cannot detect precipitates deeper inside the bulk material (dashed circle).¹³

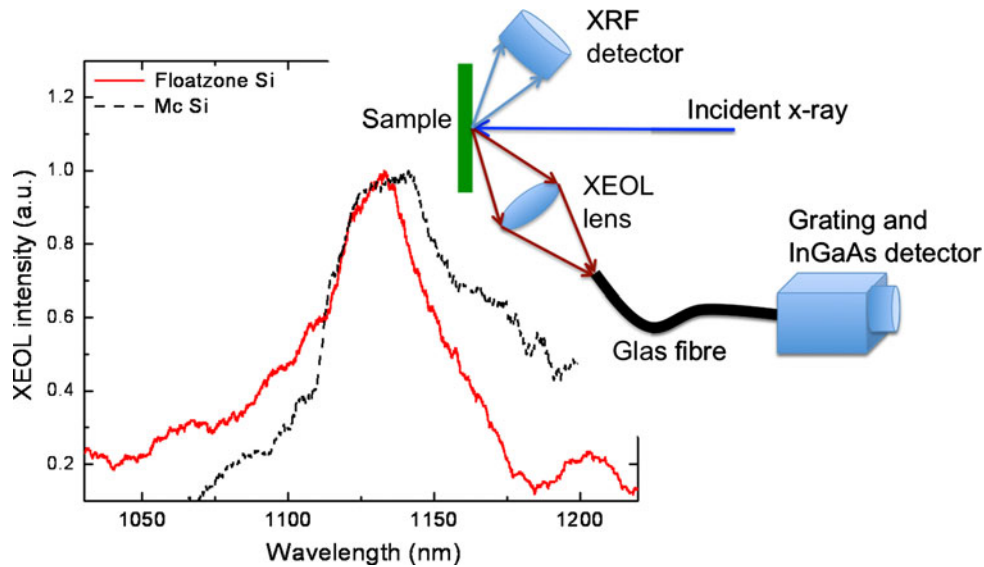


Fig. 8. Setup for x-ray excited optical luminescence. A synchrotron-generated x-ray beam excites free excess carriers, which partly recombine radiatively. The BB luminescence of both a floatzone (FZ) silicon sample and a low-quality multicrystalline (mc)-silicon sample is shown on the normalized graph.¹⁹

DISTRIBUTION OF METALLIC IMPURITIES IN MULTICRYSTALLINE SILICON

Dissolution of Metals at Extended Defects After High-Temperature Steps

Metals such as iron tend to precipitate at extended crystal defects such as grain boundaries and dislocations. Metal dissolution from these precipitates is held responsible for a decrease of

recombination lifetime after high-temperature processing steps, e.g., oxidation at 830°C to 1050°C (Fig. 1). In order to support this explanation, carrier profiles over several grains have been analyzed on a pregettered multicrystalline (mc)-silicon wafer after oxidation.²¹ Two models, both considering homogeneously distributed defects within the grains and the recombination activity of grain boundaries, have been fitted to the experimental data (Fig. 9): (i) a

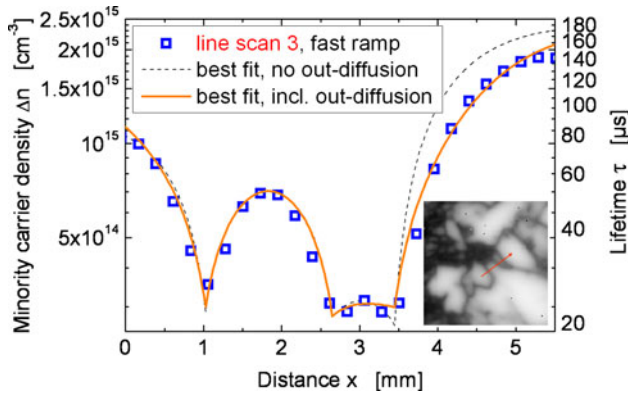


Fig. 9. Line-scan lifetime image over different grains (squares) and fits of two diffusion models. The first model (dashed line) only takes carrier diffusion into account, whereas the second model (solid line) additionally considers outdiffusion of iron atoms from precipitates situated at grain boundaries.²¹

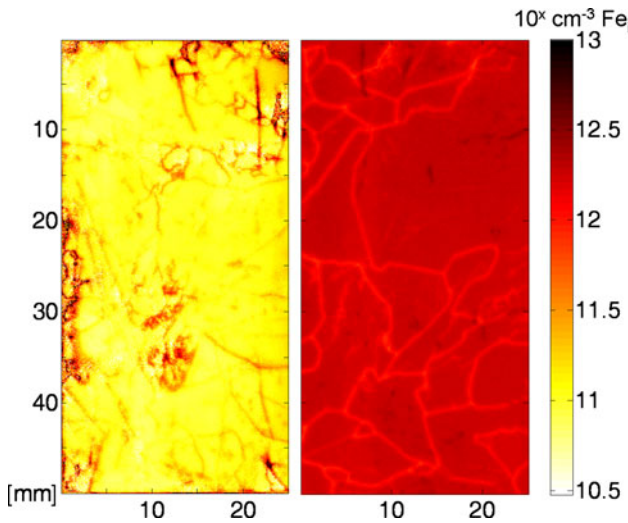


Fig. 10. Comparison of distribution of iron point defects between lightly (left) and heavily (right) contaminated multicrystalline silicon (as-grown, SiN-passivated). Note the different behavior of grain boundaries in both cases.

simple model where only carrier diffusion is taken into account (black dashed line) fits well for small grains but fails for the large grain on the right side (at 3.5 mm to 5.5 mm distance); (ii) the advanced model also takes outdiffusion of iron from the grain boundaries into account and fits well to the experimental data. Iron has been chosen for the model due to the results of global quasi-steady-state photoconductance (QSSPC) measurements on this sample, revealing iron to be the dominant recombination center.

Simulation of the Iron Concentration After Block Crystallization

An example of a more systematic approach to access the distribution of, e.g., iron in multicrystalline silicon is presented in this paragraph. A two-

dimensional (2D) numerical simulation tool has been set up within the Sentaurus Process^{®22} platform. The distribution of both precipitated and interstitial iron after crystallization is simulated by a model based on the Fokker–Planck equation and a precipitation model by Haariltunen.²³ A central element of our simulation is the consideration of differences in iron solubility depending on the dislocation density DL . We approximate this dependency in a linear ansatz: starting from precipitates of the size of n_i atoms, time-dependent dissolution and generation rates, $d(n_i, t)$ and $g(n_i, t)$, respectively, are defined. They are assumed to be proportional to the iron diffusivity D , the iron solubility C_{sol} , and the interstitial iron concentration $[Fe_i]$, respectively.

$$d(n_i, t) \propto D \times C_{sol} \times \exp(E_a / (kTn_i^{1/2}));$$

$$C_{sol} = C_{sol}(DL = 0) \times (1 + DL \times 8.9 \times 10^{-7} / kT)$$

$$g(n_i, t) \propto D \times [Fe_i]. \quad (1)$$

Please refer to Ref. 24 for a description of the complete model.

This model has been used to explain the experimental results shown in Fig. 10. The iron point defect density has been measured for two silicon samples, one from a block with low iron concentration and one with additional intentional iron contamination of 20 ppm. As expected, the lightly contaminated sample showed significantly lower interstitial iron concentration compared with the heavily contaminated sample. A striking difference, however, is found in the spatial distribution: in the lightly contaminated sample, the interstitial iron concentration in the vicinity of the grain boundary is higher than inside the grain, whereas in the heavily contaminated sample the highest interstitial iron concentration is found inside the grains.

In order to explain this effect, the iron distribution after crystallization has been simulated for adjacent areas of low, middle, and high dislocation density (10^4 cm^{-2} , $4 \times 10^5 \text{ cm}^{-2}$, and $4 \times 10^6 \text{ cm}^{-2}$, respectively; Fig. 11). Consistent with the experimental data from Fig. 10, the Fe_i concentration gradient from lightly to heavily dislocated areas is dependent on the contamination level.

This reflects the parallel occurrence of two different effects: (i) precipitation is increased in areas with higher dislocation density, which reduces the concentration of interstitial iron; and (ii) the solubility of iron in heavily dislocated areas exceeds the solubility in lightly dislocated areas. Depending on the contamination level, one of these two effects is dominant. Note that in both cases the total iron concentration (interstitial and precipitated iron) is highest in areas of high dislocation density.

REVERSE BREAKDOWN

In addition to reducing the recombination lifetime and thus the material quality, metals may, in the

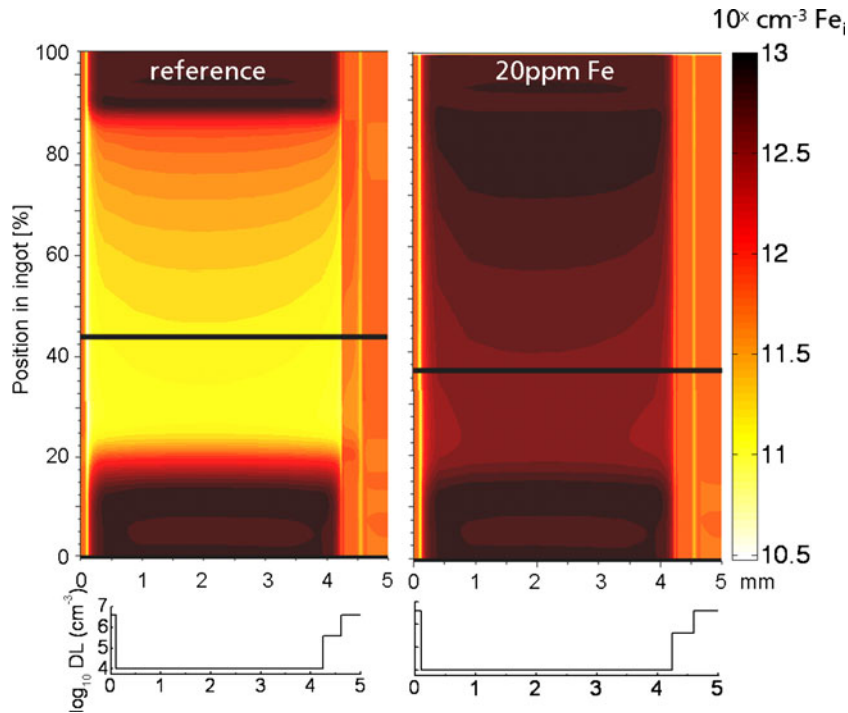


Fig. 11. Numerical simulation (2D) of iron point defect distribution after block crystallization for low (*left*) and high (*right*) iron concentration. The images show the Fe_i concentration over a whole ingot for an idealized grain of about 4 mm grain size with adjacent areas of medium and high dislocation density (according to line scans below the simulation results). The ingot heights of the measured wafers in Fig. 10 are marked with black lines. Consistent with the experimental data from Fig. 10, the Fe_i concentration gradient from lightly to heavily dislocated areas is dependent on the contamination level.²⁴

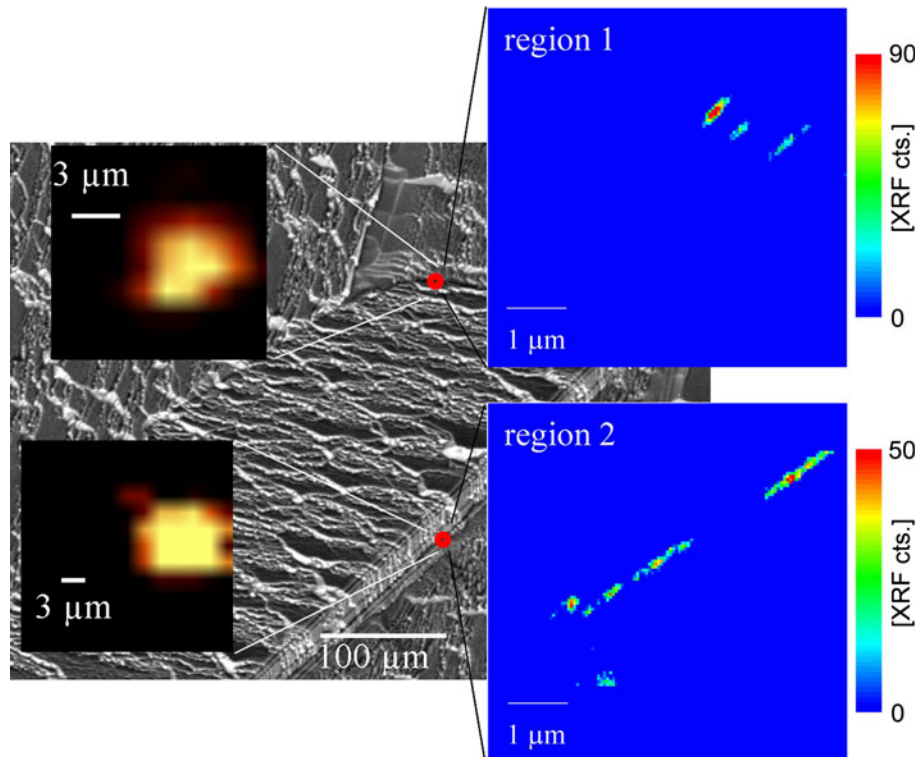


Fig. 12. μ -XRF measurements (*right insets*) at positions showing reverse breakdown. The breakdown positions have been identified by electroluminescence spectroscopy (-10 V reverse bias, *left insets*) with precision of approximately $1 \mu\text{m}$. No other precipitates have been found along grain boundaries.²⁷

form of precipitates, create centers of preferential electrical diode breakdown. Cells may be subject to reverse voltage exceeding 10 V when a single cell in a module is shaded (e.g., by leaves or snow). Current densities and thus power dissipation at breakdown spots may become large, which may result in thermal destruction of the cell or the module. Three types of breakdown have been identified, with different voltage characteristics^{25,26} and different origins. This paper focuses on soft breakdown sites (called type II), which are related to metal impurities.

Soft breakdown sites have been localized by electroluminescence imaging. Position and size have been determined by high-resolution luminescence spectroscopy with precision of approximately 1 μm . $\mu\text{-XRF}$ measurements at beamline ID22NI at the ESRF synchrotron have revealed the existence of iron precipitates at the breakdown positions (Fig. 12). No precipitates have been found at other positions along grain boundaries.

Possible mechanisms leading to the detected type of breakdown may be related to trap-assisted tunneling or ionization processes over intermediate defect levels induced by iron precipitates. More likely, however, is a change of the electric field due to location of the iron (silicide) precipitates in the space-charge region, which facilitates breakdown at reverse bias. A detailed analysis may be found in Ref. 27.

CONCLUSION

The spatial distribution of iron as the most frequently found metal contamination in silicon has been addressed by this survey including imaging and mapping measurement techniques. Photoluminescence and x-ray fluorescence spectra are detected for measurement of the recombination lifetime and distribution of metal precipitates, respectively. Numerical simulations of carrier diffusion have been applied to show evidence of impurity dissolution from grain boundaries after oxidation. Advanced two-dimensional simulations of the iron distribution in multicrystalline silicon blocks after crystallization are presented. It has been shown that, in addition to reducing the recombination lifetime, iron in the form of precipitates may introduce breakdown sites.

ACKNOWLEDGEMENTS

The authors gratefully acknowledge the contribution of G. Martinez-Criado, J.A. Sans, and F.D. Heinz to the synchrotron measurements as well as the preparation of bonded wafers by M. Reiche from the Max-Planck-Institute for Microstructure Physics. We are grateful for synchrotron beam time at ID22/ID22NI, granted by ESRF.

REFERENCES

- O. Schultz (PhD, Universität Konstanz, 2005).
- A.A. Istratov, T. Buonassisi, R.J. McDonald, A.R. Smith, R. Schindler, J.A. Rand, J.P. Kalejs, and E.R. Weber, *J. Appl. Phys.* 94, 6552 (2003).
- T. Buonassisi, A.A. Istratov, S. Peters, C. Ballif, J. Isenberg, S. Riepe, W. Warta, R. Schindler, G. Willeke, Z. Cai, B. Lai, and E.R. Weber, *Appl. Phys. Lett.* 87, 121918 (2005).
- T. Buonassisi, A.A. Istratov, M.D. Pickett, M. Heuer, J.P. Kalejs, G. Hahn, M.A. Marcus, B. Lai, Z. Cai, S.M. Heald, T.F. Ciszek, R.F. Clark, D.W. Cunningham, A.M. Gabor, R. Jonczyk, S. Narayanan, E. Sauar, and E.R. Weber, *Prog. Photovolt. Res. Appl.* 14, 513 (2006).
- J. Tan, D. Macdonald, N. Bennett, D. Kong, A. Cuevas, and I. Romijn, *Appl. Phys. Lett.* 91, 043505 (2007). doi: [10.1063/1.2766664](https://doi.org/10.1063/1.2766664).
- A.A. Istratov, T. Buonassisi, M.D. Pickett, M. Heuer, and E.R. Weber, *Mater. Sci. Eng. B* 134, 282 (2006).
- W. Schröter, A. Döller, A. Zozime, V. Kveder, M. Seibt, and E. Spiecker, *Solid State Phenom.* 95–96, 527 (2003).
- R.A. Bardos, T. Trupke, M.C. Schubert, and T. Roth, *Appl. Phys. Lett.* 88, 053504 (2006).
- T. Trupke, R.A. Bardos, M.C. Schubert, and W. Warta, *Appl. Phys. Lett.* 89, 44107 (2006).
- G. Zoth and W. Bergholz, *J. Appl. Phys.* 67, 6764 (1990).
- D. Macdonald, J. Tan, and T. Trupke, *J. Appl. Phys.* 103, 1 (2008).
- M.C. Schubert, M.J. Kerler, and W. Warta, *J. Appl. Phys.* 105, 114903 (2009). doi: [10.1063/1.3138805](https://doi.org/10.1063/1.3138805).
- P. Gundel, M.C. Schubert, W. Kwapil, J. Schön, M. Reiche, H. Savin, M. Yli-Koski, J.A. Sans, G. Martinez-Criado, W. Seifert, W. Warta, and E.R. Weber, *Phys. Stat. Sol. RRL* 3, 230 (2009).
- P. Gundel, M.C. Schubert, and W. Warta, *Phys. Stat. Sol. A* (2009), doi: [10.1002/pssa.200925368](https://doi.org/10.1002/pssa.200925368).
- T. Buonassisi, A.A. Istratov, M.A. Marcus, B. Lai, Z. Cai, S.M. Heald, and E.R. Weber, *Nat. Mater.* 4, 676 (2005).
- M. Kittler, X. Yu, O.F. Vyvenko, M. Birkholz, W. Seifert, M. Reiche, T. Wilhelm, T. Arguirov, A. Wolff, W. Fritzsche, and M. Seibt, *Mater. Sci. Eng. C* 26, 5 (2006).
- T.K. Sham, R. Sammynaiken, Y.J. Zhu, P. Zhang, I. Coulthard, and S.J. Naftel, *Thin Solid Films* 363, 318 (2000).
- G. Martinez-Criado, B. Alen, A. Homs, A. Somogyi, C. Miskys, J. Susini, J. Pereira-Lachataignerais, and J. Martinez-Pastor, *Appl. Phys. Lett.* 89, 221913 (2006).
- P. Gundel, G. Martinez-Criado, M.C. Schubert, J.A. Sans, W. Kwapil, W. Warta, and E.R. Weber, *Phys. Stat. Sol. RRL* 3, 275 (2009).
- O.F. Vyvenko, T. Buonassisi, A.A. Istratov, H. Hieslmaier, A.C. Thompson, R. Schindler, and E.R. Weber, *J. Appl. Phys.* 91, 3614 (2002).
- H. Habenicht, S. Riepe, O. Schultz, and W. Warta, *Proceedings of the 22nd European Photovoltaic Solar Energy Conference*, Milan, Italy (2007), p. 1519.
- Synopsys Sentaurus Process User's Manual, Release: A-2007.12, Synopsys Inc., Zurich Switzerland, www.synopsys.com, 2007.
- A. Haarahiltunen, H. Väinölä, O. Anttila, M. Yli-Koski, and J. Sinkkonen, *J. Appl. Phys.* 101, 043507/1 (2007).
- J. Schön, H. Habenicht, M.C. Schubert, and W. Warta, *Solid State Phenom.* 156–158, 223 (2009).
- W. Kwapil, M. Kasemann, P. Gundel, M.C. Schubert, W. Warta, P. Bronsveld, and G. Coletti, *J. Appl. Phys.* 106, 063530 (2009).
- W. Kwapil, M. Kasemann, J. Giesecke, B. Michl, and W. Warta, *Proceedings of the 23rd European Photovoltaic Solar Energy Conference*, Valencia, Spain, (2008).
- W. Kwapil, P. Gundel, M.C. Schubert, F.D. Heinz, W. Warta, E.R. Weber, A. Goetzberger, and G. Martinez-Criado, *Appl. Phys. Lett.* 95, 232113 (2009).